Ca_V3.3 T-type calcium channels contribute to carboplatin resistance in retinoblastoma

Sooyun Kim[1,2,3,*], **Chang Sik Cho**[1,2], **Ha Young Jang**[1,2], **Dong Hyun Jo**[2,4], **and Jeong-Hun Kim**[1,2,3,5,*]

From the [1]*Fight Against Angiogenesis-Related Blindness (FARB) Laboratory, Clinical Research Institute, Seoul National University Hospital, Seoul, Republic of Korea;* [2]*Global Excellence Center for Gene & Cell Therapy (GEC-GCT), Seoul National University Hospital, Seoul, Republic of Korea;* [3]*Institute of Reproductive Medicine and Population, Seoul National University College of Medicine, Seoul, Republic of Korea;* [4]*Department of Anatomy & Cell Biology, Seoul National University College of Medicine, Seoul, Republic of Korea;* [5]*Department of Biomedical Sciences & Ophthalmology, Seoul National University College of Medicine, Seoul, Republic of Korea*

Reviewed by members of the JBC Editorial Board. Edited by Mike Shipston

Carboplatin resistance in retinoblastoma, an aggressive pediatric intraocular tumor, remains a major clinical challenge in treatment. This study elucidates the role of T-type calcium channels in carboplatin resistance using human retinoblastoma Y79 cells. We generated carboplatin-resistant Y79 (Y79CR) cells and characterized their electrophysiological properties. Patch-clamp recordings revealed a subpopulation of enlarged Y79CR cells (*i.e.*, giant cells) with hyperpolarized resting membrane potentials, reduced input resistance, and increased T-type calcium currents. Quantitative RT-PCR analysis confirmed upregulation of $Ca_V3.3$ mRNA in Y79CR cells, identifying $Ca_V3.3$ as the predominant channel mediating these currents. Pharmacological inhibition of $Ca_V3.3$ using ML218 and TAT-C3P attenuated the sustained currents and partially restored carboplatin sensitivity, as evidenced by decreased IC_{50} values in Y79CR cells. These findings demonstrate a critical role for T-type calcium channels, particularly $Ca_V3.3$, in mediating chemoresistance in retinoblastoma. Our results suggest that targeting these channels may provide a potential strategy to enhance the efficacy of carboplatin-based therapy in retinoblastoma treatment.

Retinoblastoma is the most prevalent and aggressive pediatric retinal cancer, presenting substantial challenges in treatment and management (1, 2, 3). Carboplatin, a platinum-based chemotherapeutic agent, is widely used as a first-line treatment due to its efficacy in reducing tumor size and preventing metastasis (1). However, the development of chemoresistance during long-term carboplatin treatment complicates retinoblastoma management, necessitating a deeper understanding of the underlying mechanisms (4).

Recent studies highlight the role of polyploid giant cancer cells in chemoresistance across various cancers (5, 6). Enlarged cells have also been documented in retinoblastoma (7, 8), and our previous work with the human Y79 retinoblastoma cell line identified a subset of these enlarged "giant" cancer cells

(9), suggesting a potential link between cell morphology and drug resistance in retinoblastoma.

Our earlier studies revealed that these giant cells in Y79 cell populations exhibit enhanced electrical maturity and a higher density of active T-type calcium channels (9). T-type calcium channels, which include the $Ca_V3.1$, $Ca_V3.2$, and $Ca_V3.3$ subtypes, have emerged as key players in chemoresistance (10, 11), regulating cancer cell growth, proliferation, and survival (12, 13). Inhibition of these channels has been shown to sensitize cancer cells to chemotherapeutic agents, including carboplatin, by enhancing apoptosis (11, 14, 15). However, the specific role of T-type calcium channel in retinoblastoma chemoresistance remains unexplored.

Given the enhanced T-type calcium channel activity observed in giant Y79 cells, combined with emerging evidence of these channels' involvement in chemoresistance, we hypothesize that $Ca_V3.3$ channels play a crucial role in carboplatin resistance in retinoblastoma. This study aims to explore the functional expression and role of $Ca_V3.3$ channels in carboplatin-resistant Y79 (Y79CR) retinoblastoma cells. By investigating the connection between enlarged cells, $Ca_V3.3$ activity, and carboplatin resistance, we seek to identify new therapeutic targets for improving treatment efficacy.

Results

Y79CR cells exhibit an increased proportion of large-diameter cells

To investigate the role of giant cells in carboplatin resistance, we generated Y79CR cells by exposing parental Y79 cells to increasing doses of carboplatin over multiple rounds (4). 3-(4,5-dimethylthiazol-2-yl)-2,5-diphenyltetrazolium bromide assays showed that Y79CR cells exhibited nearly fourfold reduced sensitivity to carboplatin compared to parental cells (IC_{50}: parental Y79, 72.5 ± 44.1 μM; Y79CR, 282.8 ± 240.4 μM; $n = 10$, $p < 0.0002$, U test; Fig. 1A). This increase in IC_{50} confirms the development of carboplatin resistance in the Y79CR cells.

Notably, Y79CR cells showed a significantly higher proportion of large-diameter cells than parental Y79 cells (Fig. 1, B

* For correspondence: Jeong-Hun Kim, steph25@snu.ac.kr; Sooyun Kim, sooyun.k@gmail.com.
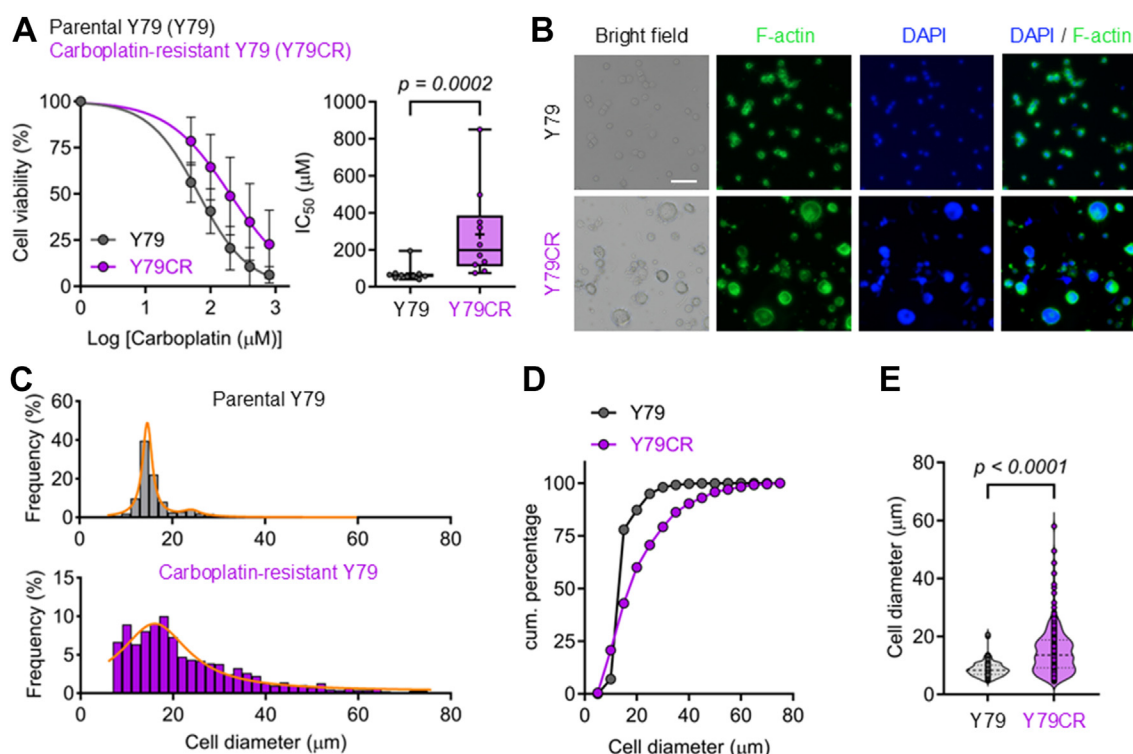
Figure 1. Characterization of carboplatin resistance in Y79 cells and its association with large-diameter cells. *A, left*: dose-response curves for parental Y79 and carboplatin-resistant Y79 (Y79CR) cells, used to calculate IC$_{50}$ values. *Right*: quantification of IC$_{50}$ values showing significantly increased carboplatin resistance in Y79CR cells ($p = 0.0002$). *B*, representative bright-field and fluorescence images of Y79 (*top*) and Y79CR (*bottom*) cells stained for F-actin (*green*) and nuclei (DAPI, *blue*). The scale bar represents 50 μm. Y79CR cells exhibit a higher prevalence of large-diameter cells, with clear morphological differences than parental Y79 cells. *C*, histograms of cell diameter distributions. Parental Y79 cells (*top*) show a narrower distribution, while Y79CR cells (*bottom*) have a broader and skewed distribution toward larger diameters, indicating an increased proportion of large-diameter cells. *D*, cumulative percentage plot comparing cell diameter distributions between parental Y79 and Y79CR cells. The Kolmogorov–Smirnov test shows a significant difference between the two populations ($p < 0.0001$). *E*, violin plot showing the distribution of cell diameters in parental and Y79CR populations Y79CR cells have a significantly larger average diameter than parental cells, supporting the association between cell enlargement and carboplatin resistance. Data are presented as mean ± SD. DAPI, 4,6-diamidino-2-phenylindole dihydrochloride.

and *C*). The distribution of cell diameters in Y79CR cells shifted toward larger sizes, showing a broader and more heterogeneous range (Fig. 1*C*). Quantitative analysis confirmed that Y79CR cells had a significantly larger average diameter than parental Y79 cells ($p < 0.0001$, Kolmogorov–Smirnov test; Fig. 1*D*). Specifically, Y79CR cells averaged 15.0 ± 8.3 μm in diameter, compared to 8.8 ± 2.8 μm in parental cells ($p < 0.0001$, *U* test; Fig. 1*E*), suggesting that cell enlargement is associated with carboplatin resistance.

Two distinct Y79CR cell populations show different electrophysiological properties

Intrinsic membrane properties, such as resting membrane potential (RMP) and input resistance, are key indicators of a cell's electrical maturity (16, 17). Given that retinoblastoma cells are electrically active (18, 9), we characterized these properties to identify Y79CR cell subpopulations more precisely. We performed whole-cell patch-clamp recordings and found a correlation between cell size, RMPs, and input resistance in Y79CR cells (Fig. 2, *A* and *B*). Using K-means clustering analysis based on cell diameter and RMP, we identified two distinct subpopulations: "regular" and "giant" cells (Fig. 2*C*).

Giant Y79CR cells were significantly larger in diameter than regular cells (regular, 25.0 ± 8.0 μm, $n = 25$; giant,

51.9 ± 12.5 μm, $n = 68$; $p < 0.0001$, *U* test; Fig. 2*D*, Table S1). They also exhibited more hyperpolarized RMPs (regular, −16.7 ± 8.4 mV, $n = 25$; giant, −39.5 ± 9.3 mV, $n = 68$; $p < 0.0001$, *U* test; Fig. 2*D*) and significantly lower input resistances (regular, 1370.2 ± 807.4 MΩ, $n = 23$; giant, 601.9 ± 292.5 MΩ, $n = 68$; $p < 0.0001$, *U* test; Fig. 2*D*, Table S1), suggesting enhanced electrical maturity in the giant cells. The inverse relationship between cell size and input resistance implies that giant cells have more ion channels, contributing to their lower input resistance.

Sustained T-type Ca^{2+} currents are enhanced in giant Y79CR cells

Next, we evaluated the functional expression of T-type Ca^{2+} channels in Y79CR cells of different sizes using whole-cell current recordings. Ca^{2+} currents were elicited using 200-ms voltage step depolarization from −120 mV to −40 mV from a holding potential of −120 mV at a frequency of 0.2 Hz. Strikingly, we observed a pronounced difference in Ca^{2+} current profiles between regular and giant cells (Fig. 3*A*). While both cell types exhibited a rapidly activating and inactivating transient peak, only giant cells displayed a prominent, gradually inactivating sustained component (Fig. 3, *A* and *B*). This finding is supported by previous studies indicating that among
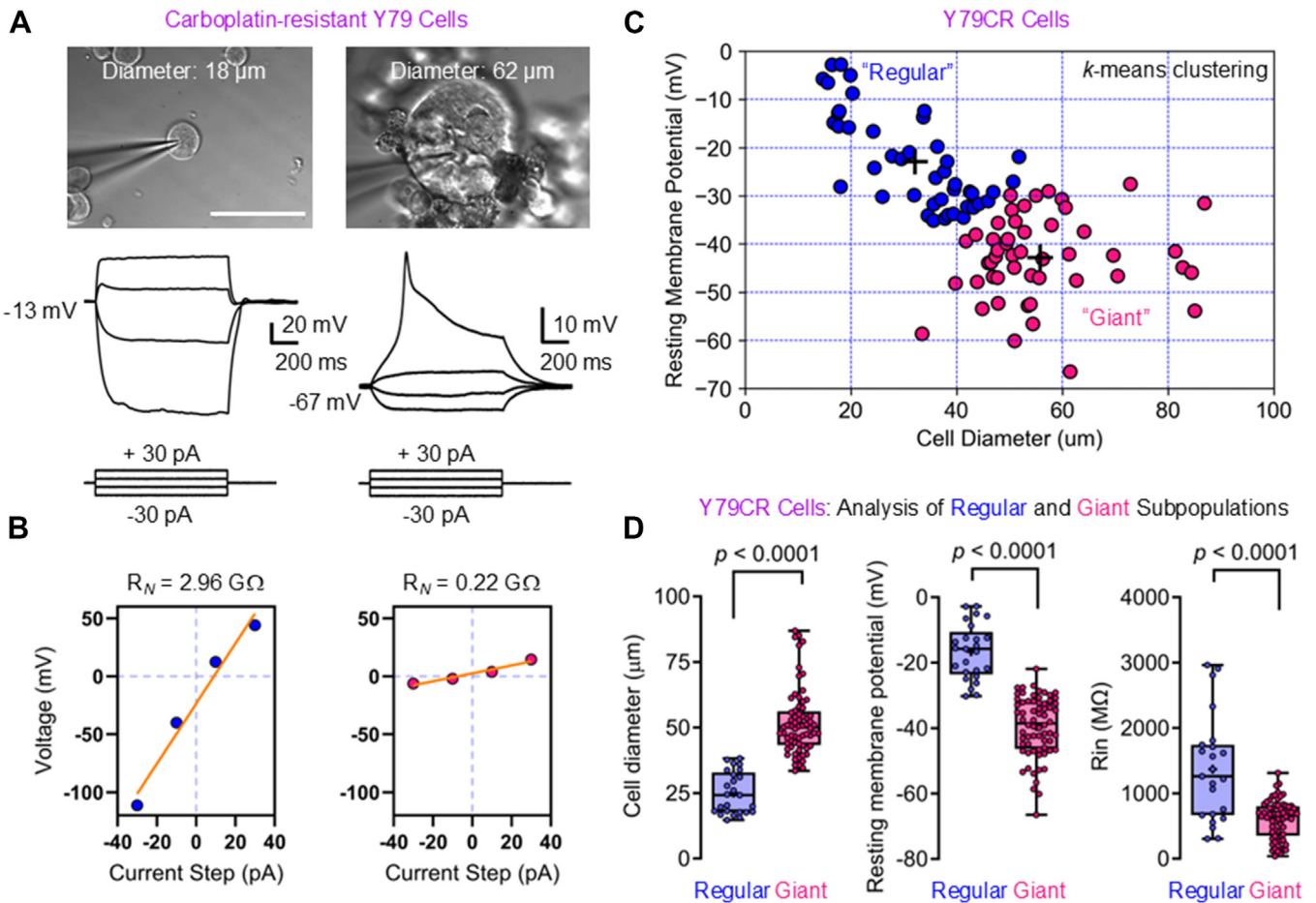
Figure 2. Electrophysiological properties of regular and giant Y79CR cells. *A, top*: bright-field images of Y79CR cells with small (18 μm) and large (62 μm) diameters. The scale bar represents 50 μm. *Bottom*: voltage responses to current step injections from −30 to +30 pA at resting membrane potentials of −13 mV (*left*) and −67 mV (*right*), showing distinct electrophysiological behaviors between the two cell types. *B*, voltage-current (V-I) responses for the small and large Y79CR cells shown in *panel A*. Input resistance was calculated from the slope of the linear regression (*yellow; left*: 2.96 GΩ; *right*: 0.22 GΩ). *C*, unsupervised k-means clustering of Y79CR cells based on cell diameter and resting membrane potential, revealing two distinct populations: "regular" (*blue*) and "giant" (*magenta*). The centroids (+) represent the centers of the clusters. In the following figures, *blue and magenta colors* represent regular and giant Y79CR cell subpopulation, respectively. *D*, quantitative comparison of regular and giant cell properties. *Left*: cell diameter. *Middle*: resting membrane potential. *Right*: input resistance (R_in). Giant cells show significantly larger diameter, more hyperpolarized resting potential, and lower input resistance ($p < 0.0001$ for all comparisons). Box plots show median, quartiles, and individual data points ($n = 25$ biological replicates from independent experiments, with 1–11 technical replicates per experiment representing individual cells). All data are presented as mean ± SD. Y79CR, carboplatin-resistant Y79.
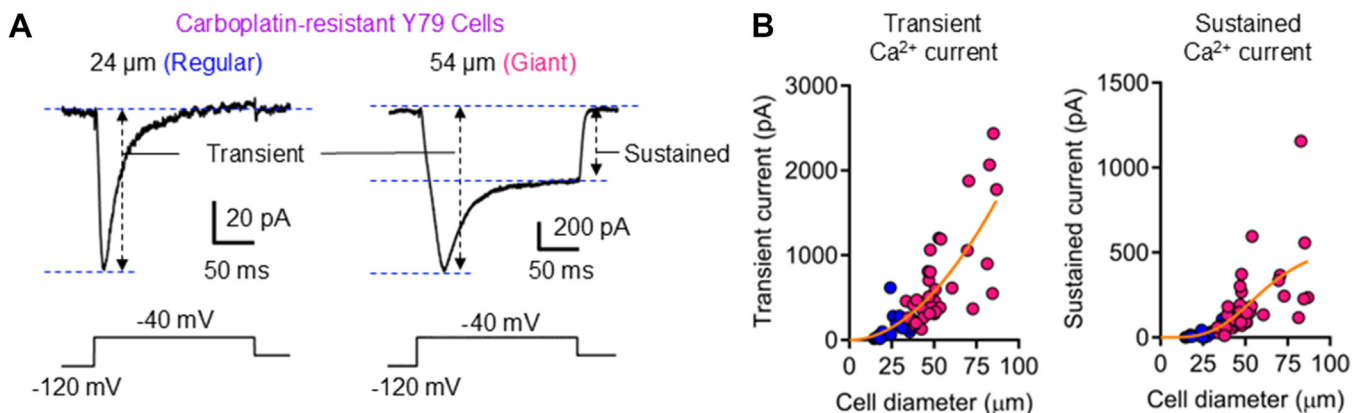

Figure 3. Sustained calcium currents are prominent in giant Y79CR cells. *A*, low-voltage activated (−40 mV) calcium currents recorded in regular (24 μm) and giant (54 μm) Y79CR cells. Inward currents were analyzed as transient and sustained components, showing distinct behaviors between the two cell types. *B, left*: peak amplitude of transient inward currents increases with cell diameter, showing larger currents in giant cells. *Right*: sustained currents are minimal in regular cells but significantly elevated in giant cells, indicating distinct regulation in giant cells. Each dot represents an individual cell measurement, with *yellow curves* illustrating the trend in the data. Y79CR, carboplatin-resistant Y79.

the three low voltage-gated T-type Ca^{2+} channel subtypes (Ca$_V$3.1, Ca$_V$3.2, and Ca$_V$3.3); Ca$_V$3.3 exhibits the slowest inactivation kinetics, which is consistent with the sustained calcium currents observed in giant cells ([19]). The amplitude of both the transient and sustained components increased with cell size, but the difference was particularly pronounced for the sustained component (Fig. 3*B*). While regular cells showed negligible sustained currents across all sizes, giant cells exhibited a substantial increase in sustained Ca^{2+} currents. This stark contrast in sustained current profiles between regular and giant cells suggests a fundamental difference in their calcium channel expression or regulation, potentially contributing to their distinct phenotypes and responses to carboplatin.

Involvement of Ca$_V$3.3 channels in sustaining Ca^{2+} currents in giant Y79CR cells

To explore the role of Ca$_V$3.3 channels in sustained Ca^{2+} currents in giant Y79CR cells, we used two pharmacological approaches. First, we applied ML218, a potent inhibitor of the Ca$_V$3.2 and Ca$_V$3.3 channels ([20], [21]). ML218 effectively reduced the sustained current in giant cells in giant cells (sustained: control, 276.0 ± 159.9 pA; ML218, 65.5 ± 69.6 pA, $n = 6$, $p < 0.03$, Wilcoxon-signed rank test; Fig. 4*A*). While the total peak current showed some reduction, the isolated transient component (obtained by subtracting the sustained component) remained largely unchanged (subtracted current: control, 754.2 ± 420.6 pA; ML218, 596.7 ± 464.3 pA; $n = 6$, $p = 0.09$, Wilcoxon-signed rank test; Fig. 4*A*). To further confirm the involvement of Ca$_V$3.3 channels, we used TAT-C3P, a peptide that selectively reduces Ca$_V$3.3 channel activity ([22]). The sustained Ca^{2+} currents, which were prominent in control giant cells, were nearly abolished when TAT-C3P was applied intracellularly (sustained current reduction: regular, 9.8 ± 12.7 pA, $n = 13$; giant, 174.6 ± 106.5 pA, $n = 12$; TAT-C3P–treated giant, 76.3 ± 81.0 pA, $n = 10$; regular *versus* giant, $p < 0.0001$, *U* test; giant *versus*. TAT-C3P–treated giant, $p = 0.01$, *U* test; Fig. 4*B*). These results confirm that Ca$_V$3.3 channels are important for maintaining sustained Ca^{2+} currents in giant Y79CR cells.

Additionally, we examined the voltage dependence and kinetic properties of Ca^{2+} currents in Y79CR cells to characterize the T-type calcium channels further. Both steady-state activation and inactivation curves shifted to more negative potentials in giant cells compared to regular cells (activation: regular, $V_{0.5} = -44.4 ± 5.9$ mV, $n = 8$; giant, $V_{0.5} = -57.6 ± 6.0$ mV, $n = 17$; regular *versus* giant, $p < 0.0001$, *U* test; inactivation: regular, $V_{0.5} = -54.0 ± 7.7$ mV, $n = 5$; giant, $V_{0.5} = -65.0 ± 8.6$ mV, $n = 15$; regular *versus* giant, $p = 0.0328$, *U* test; Fig. 4, *C* and *D*, Table S2). These shifts are consistent with the biophysical properties of Ca$_V$3.3 channels and suggest their increased functional expression in giant Y79CR cells ([19]). Remarkably, when we applied TAT-C3P to giant cells, we observed a reversal of this shift. The activation and inactivation curves returned to values similar to those of regular cells

(activation: TAT-C3P–treated giant, $V_{0.5} = -47.9 ± 4.7$ mV, $n = 12$; giant *versus* TAT-C3P–treated giant, $p < 0.0001$, *U* test; inactivation: TAT-C3P–treated giant, $V_{0.5} = -58.3 ± 3.3$ mV, $n = 9$; giant *versus* TAT-C3P–treated giant, $p = 0.0177$, *U* test; Fig. 4, *C* and *D*, Table S2). This reversal strongly suggests that the observed differences in voltage dependence between regular and giant cells are primarily due to the increased expression and activity of Ca$_V$3.3 channels in giant cells.

Immunofluorescence staining confirmed elevated Ca$_V$3.3 expression in giant Y79CR cells compared to regular cells, with quantitative analysis revealing significantly higher mean fluorescence intensity in giant cells (regular: 28.2 ± 8.5 a.u., $n = 47$; giant: 45.4 ± 5.0 a.u., $n = 9$, $p < 0.0001$, *U* test; Fig. 4*E*). This molecular evidence corroborates our electrophysiological findings. Collectively, these results demonstrate that giant Y79CR cells exhibit enhanced sustained Ca^{2+} currents primarily mediated by Ca$_V$3.3 channels, which may contribute to their distinct properties and potential carboplatin resistance.

Ca$_V$3.3 inhibition resensitizes Y79CR cells to carboplatin

To establish a direct link between Ca$_V$3.3 channel activity and carboplatin resistance, we first examined the expression level of CACNA1I, which encodes the Ca$_V$3.3 channel. quantitative RT-PCR (qRT-PCR) analysis revealed significantly elevated CACNA1I mRNA levels in Y79CR cells compared to parental Y79 cells (relative expression: Y79CR, 14.0 ± 11.5, $n = 12$, $p = 0.0025$, *U* test; Fig. 5*A*). This upregulation of Ca$_V$3.3 in Y79CR cells suggests its potential involvement in the development of carboplatin resistance.

Before investigating the effects of Ca$_V$3.3 inhibition on resistant cells, we first tested whether T-type channel blockers affect the carboplatin sensitivity of parental Y79 cells (Fig. 5*B*). Neither ML218 nor TAT-C3P significantly altered the carboplatin sensitivity of parental Y79 cells (Y79: 84.8 ± 5.4 μM; Y79 + ML218: 84.0 ± 5.9 μM, $p = 0.3125$; Y79 + TAT-C3P: 69.1 ± 6.0 μM, $p = 0.063$, *U* test, $n = 5$). This indicates that T-type channel inhibition specifically affects resistant cells rather than generally modulating carboplatin sensitivity. We then examined whether inhibiting Ca$_V$3.3 channels could resensitize Y79CR cells to carboplatin using 3-(4,5-dimethylthiazol-2-yl)-2,5-diphenyltetrazolium bromide assays (Fig. 5, *C* and *D*). ML218 treatment significantly decreased the IC$_{50}$ of Y79CR cells from 171.4 ± 70.8 μM to 117.9 ± 47.2 μM ($n = 9$, $p = 0.004$, *U*-test), bringing their carboplatin sensitivity closer to that of parental Y79 cells (90.7 ± 45.1 μM). Similarly, TAT-C3P treatment reduced the IC$_{50}$ of Y79CR cells from 147.3 ± 47.0 μM to 121.6 ± 42.8 μM ($n = 11$, $p = 0.042$, *U* test). Although the reduction with TAT-C3P was less pronounced than with ML218, both treatments significantly shifted the sensitivity of Y79CR cells toward that of the parental cells (77.4 ± 7.4 μM). These findings demonstrate that inhibiting Ca$_V$3.3 channels can effectively resensitize Y79CR cells to carboplatin, suggesting that targeting Ca$_V$3.3 channels could represent a promising therapeutic strategy for overcoming chemoresistance in retinoblastoma treatment.
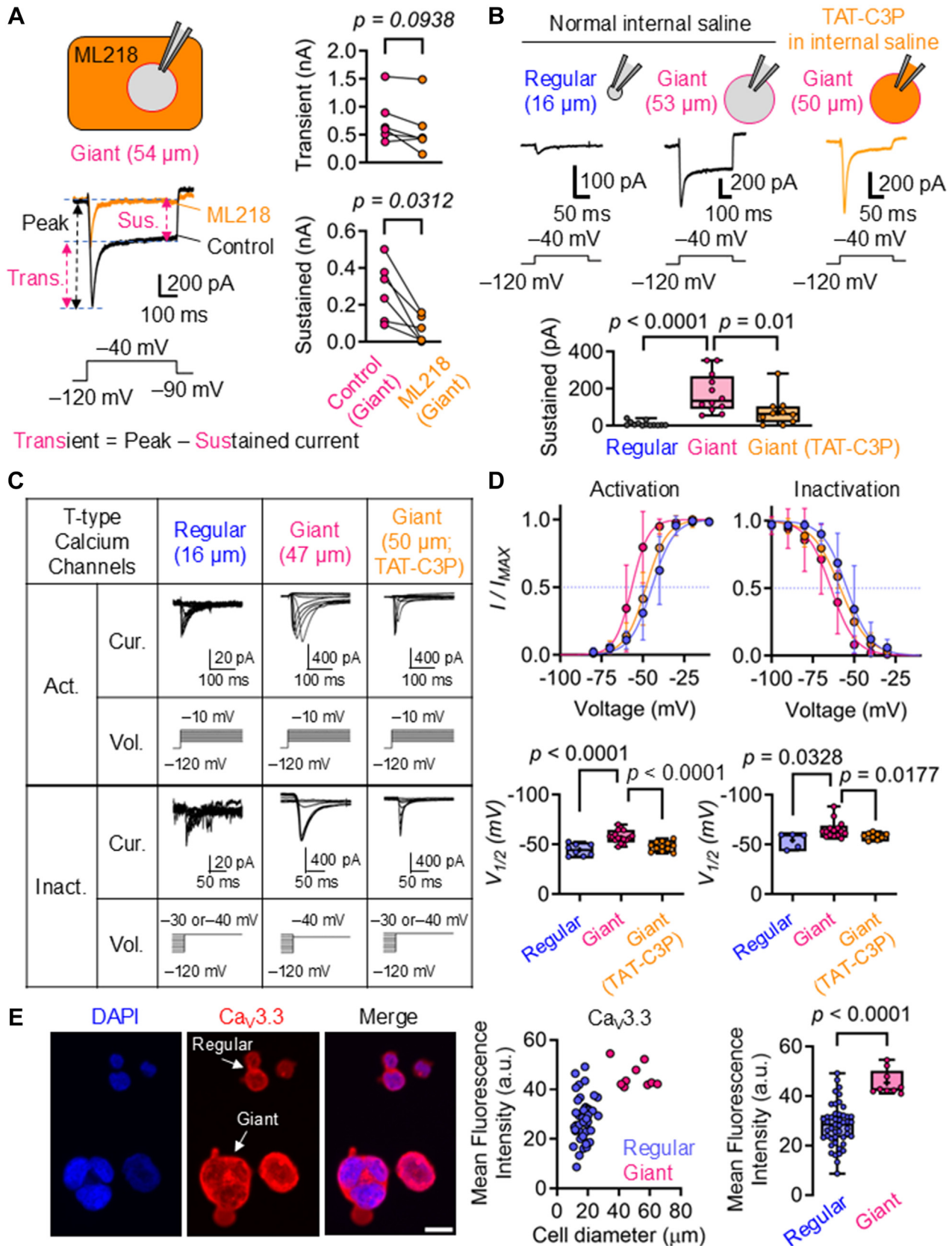
Figure 4. Pharmacological and biophysical characterization of Ca$_V$3.3 channels in Y79CR cells. *A, left*: schematic of a whole-cell patch-clamp recording from a giant Y79CR cell treated with ML218 (10–20 μM) and representative calcium currents before (Control) and after ML218 treatment recorded from a giant Y79CR cell (54 μm). *Right*: paired data showing ML218 effects on transient and sustained currents. ML218 significantly reduces the sustained current, while the transient component remains largely unchanged. Transient current was calculated by subtracting sustained from peak current. *B, top*: whole-cell recording configurations from regular (16 μm), giant (53 μm), and TAT-C3P–treated giant (50 μm) Y79CR cells. *Middle*: representative calcium current traces.
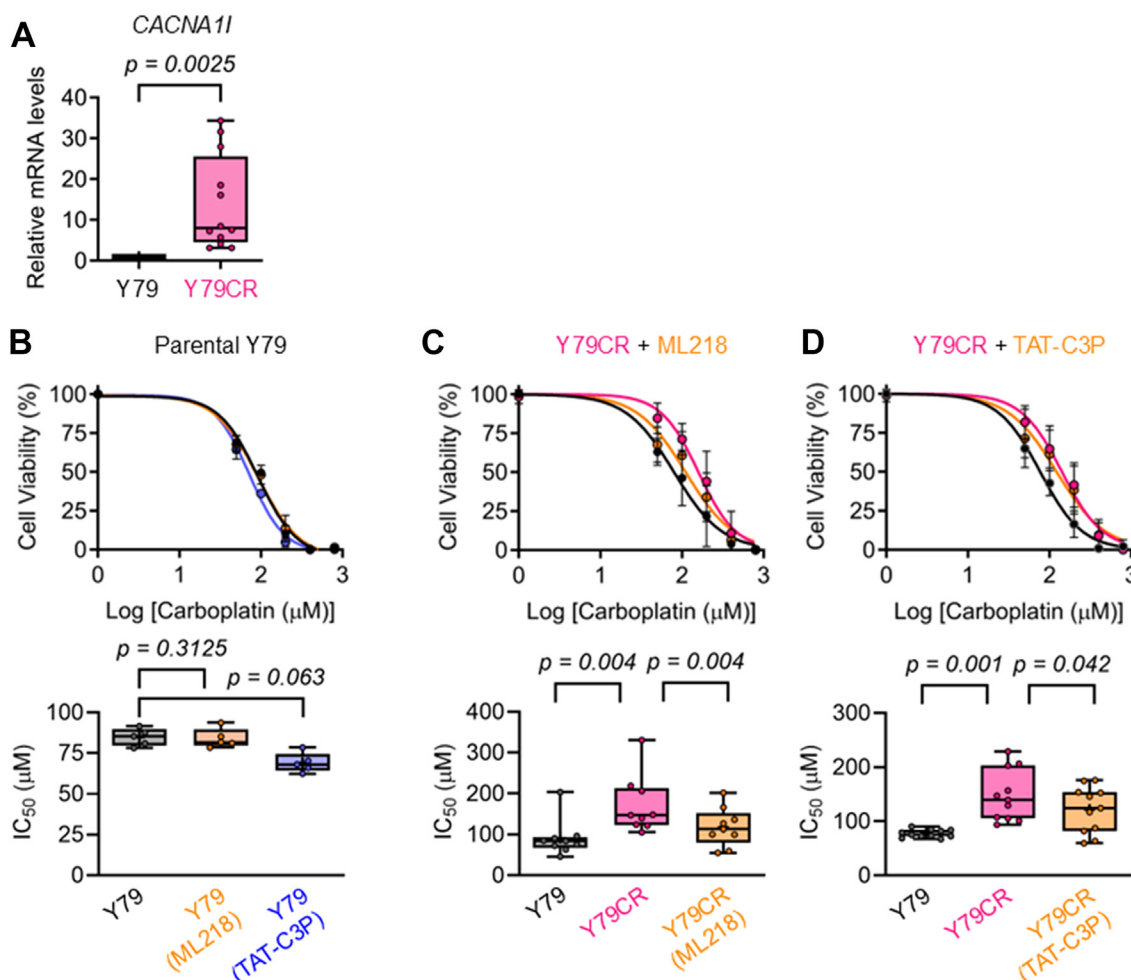
Figure 5. Ca$_V$3.3 upregulation in Y79CR cells and its role in carboplatin resistance. *A*, qRT-PCR analysis of CACNA1I (Ca$_V$3.3) mRNA levels in parental Y79 and Y79CR cells, showing significantly elevated expression in Y79CR cells (n = 12 biological replicates with technical triplicates, p = 0.0025, U test). qRT-PCR analysis performed with 12 biological replicates, each with technical triplicates. *B*, effect of T-type channel blockers on carboplatin sensitivity in parental Y79 cells. *Top*: dose-response curves for Y79 cells in control (*black*), ML218 (*orange*), or TAT-C3P (*blue*). *Bottom*: bar plot of IC$_{50}$ values showing neither ML218 nor TAT-C3P significantly altered carboplatin sensitivity (ML218: p = 0.3125; TAT-C3P: p = 0.063, U test, n = 5 independent experiments, each performed in triplicate). *C*, effect of ML218 on carboplatin sensitivity. *Top*: dose-response curves for parental Y79 (*black*), Y79CR (*magenta*), and ML218-treated Y79CR cells (*orange*). *Bottom*: bar plot of IC$_{50}$ values showing ML218 significantly decreases carboplatin resistance in Y79CR cells (n = 9 independent experiments, each performed in triplicate, p = 0.004, U test). *D*, effect of TAT-C3P on carboplatin sensitivity. *Top*: dose-response curves for parental Y79 (*black*), Y79CR (*magenta*), and TAT-C3P–treated Y79CR cells (*orange*). *Bottom*: bar plot of IC$_{50}$ values showing TAT-C3P significantly reduces carboplatin resistance in Y79CR cells (n = 11 independent experiments, each performed in triplicate, p = 0.042, U test). All data are presented as mean ± SD. Y79CR, carboplatin-resistant Y79; qRT-PCR, quantitative RT-PCR.

Discussion

Our study identifies Ca$_V$3.3 T-type calcium channels as a key factor in the development of carboplatin resistance in human retinoblastoma Y79 cells. We observed an increased proportion of giant cells in Y79CR cells, characterized by hyperpolarized resting membrane potentials, low-input resistance, and a higher density of sustained T-type Ca^{2+} currents. Pharmacological inhibition of these channels significantly reduced calcium currents and resensitized cells

to carboplatin, highlighting the crucial role of Ca$_V$3.3 in chemoresistance.

The overexpression of Ca$_V$3.3 T-type Ca^{2+} channels in giant Y79CR cells and their contribution to the chemoresistant phenotype corroborate previous studies demonstrating the involvement of T-type Ca^{2+} channels in chemoresistance in other cancers (23). Our findings show the potential of targeting Ca$_V$3.3 as a therapeutic strategy in retinoblastoma. It is worth noting that while Ca$_V$3.3 was significantly upregulated

---

Bottom: quantification of sustained calcium currents. *C*, representative current traces showing voltage-dependent activation (*top*) and inactivation (*bottom*) from regular (16 μm), giant (47 μm), and TAT-C3P–treated giant (50 μm) Y79CR cells. Voltage protocols shown below traces. *D*, *top*: normalized activation and steady-state inactivation curves for regular (*blue*), giant (*magenta*), and TAT-C3P–treated giant (*orange*) cells. *Bottom*: V$_{1/2}$ values for activation and inactivation. Data points represent mean ± SD, with curves fitted using the Boltzmann function. Detailed fit parameters in Table S2. *E*, *left*: immunofluorescence images showing DAPI (*blue*) and Ca$_V$3.3 (*red*) staining. The scale bar represents 20 μm. *Middle*: scatter plot of Ca$_V$3.3 fluorescence intensity *versus* cell diameter. *Right*: quantification showing significantly higher Ca$_V$3.3 expression in giant cells than regular cells (p < 0.0001, U test; data from 3 biological replicates with multiple cells analyzed per experiment). Data are presented as mean ± SD. Y79CR, carboplatin-resistant Y79; DAPI, 4,6-diamidino-2-phenylindole dihydrochloride.

in Y79CR cells, the expression levels of Ca$_V$3.1 and Ca$_V$3.2 were slightly decreased (Fig. S2*A*). This selective upregulation of Ca$_V$3.3, coupled with its functional contribution to the chemoresistant phenotype, suggests a specific role for this isoform in retinoblastoma, differentiating it from other T-type calcium channels.

Interestingly, our results also suggest a possible interplay between Ca$_V$3.3 channels and the previously identified FoxM1–ABCC4 axis in mediating carboplatin resistance. FoxM1 upregulates ABCC4, a drug efflux transporter, promoting Y79CR cells (24). Given that T-type calcium channels regulate FoxM1 expression (11), our findings point to a potentially complex regulatory network involving calcium signaling, transcription factors, and drug efflux pumps. Further investigation of this network may reveal additional therapeutic targets and strategies for overcoming chemoresistance.

Our study revealed that TAT-C3P directly inhibited Ca$_V$3.3 channel activity when applied through the patch pipette. This finding contrasts with previous work by Cmarko and Weiss (22), who reported no immediate effects under similar conditions. While the exact reasons for this discrepancy are not yet clear, it may be attributed to differences in experimental setup, cell types, or other unidentified factors. Our results suggest that TAT-C3P's effects on Ca$_V$3.3 channels may be more direct than previously thought, at least in certain contexts. These findings highlight the need for further investigation into the mechanisms of TAT-C3P's action and the specific conditions influencing its modulation of Ca$_V$3.3 activity. Future studies using genetic approaches, such as CRISPR/Cas9-mediated knockdown of Ca$_V$3.3, could provide clearer evidence of its role in carboplatin resistance and the broader chemoresistance mechanism.

These findings have significant implications for retinoblastoma treatment. Developing Ca$_V$3.3-specific inhibitors could provide a new strategy for overcoming carboplatin resistance. However, before clinical translation, *in vivo* studies are necessary to validate these findings, considering the tumor microenvironment and potential systemic effects of Ca$_V$3.3 inhibition. Although our qRT-PCR results showed a slight decrease in Ca$_V$3.1 and Ca$_V$3.2 expression in Y79CR cells, the functional significance of these changes remains to be fully explored. Additionally, the molecular mechanisms linking Ca$_V$3.3 activity to carboplatin resistance, including interactions with the FoxM1–ABCC4 axis, require further elucidation. Understanding these mechanisms may reveal additional therapeutic targets and offer a more comprehensive approach to overcoming chemoresistance.

Experimental procedures

Cell culture

Human Y79 retinoblastoma cells (ATCC) were obtained directly from ATCC and maintained according to the supplier's guidelines. Cells were cultured in RPMI-1640 medium (WelGene) supplemented with 10% fetal calf serum (Gibco-BRL) and 100 µg/ml streptomycin (Invitrogen) at 37 °C in a 5% CO$_2$ atmosphere. As Y79 is a suspension cell line, cell density

was regularly monitored and maintained between 0.5 and 1×10^6 cells/ml to ensure consistent growth conditions. Y79CR cells were generated as previously described (4) and maintained in medium containing 5 to 10 µM carboplatin (Sigma-Aldrich, Cat. No. C2538).

Cell viability assay

Cell viability was assessed using an EZ-Cytox assay kit (DoGenBio). A total of 1 to 5×10^4 cells/well were seeded in 96-well plates and cultured overnight. The next day, cells were treated with varying concentrations of carboplatin (50–800 µM) and incubated for 48 h. The WST-1 solution was added to each well and incubated at 37 °C for 3 to 4 h. Absorbance was measured at 450 nm using a microplate reader (Molecular Devices). Each experiment was performed in triplicate. For drug combination studies, cells were initially treated with respective doses of T-type Ca^{2+} channel blockers for 24 h. Subsequently, media containing the blockers were replaced with media containing the indicated concentrations of carboplatin for an additional 48 h.

Immunofluorescence

Cells were fixed in 4% paraformaldehyde solution in 100 mM PBS, pH 7.4, for 15 min at room temperature. After fixation, cells were permeabilized with 0.25% Triton X-100 (Sigma-Aldrich, Cat. No. T8787) and blocked with 1% bovine serum albumin in PBS for 30 min to minimize background staining. For filamentous actin (F-actin) visualization, cells were stained with Alexa Fluor 488 phalloidin (Thermo Fisher Scientific, Cat. No. A12379). Nuclear staining was performed using 4′,6-diamidino-2-phenylindole dihydrochloride (1:5000; Sigma-Aldrich, Cat. No. D9542). To detect Ca$_V$3.3 (CACNA1I), cells were incubated with anti-Ca$_V$3.3 antibody (1:200; Alomone Labs, Cat. No. ACC-009), followed by species-specific Alexa Fluor 594 IgG (1:500; Invitrogen, Cat. No. A-11037).

Patch-clamp recordings

Cells were recorded on 18-mm poly-D-lysine–coated coverslips (Marienfeld Superior, Cat. No. 0111580) and superfused with buffered Ames' medium at a rate of 4 to 5 ml/min. Electrical signals were acquired using a patch-clamp amplifier (Multiclamp 700B, Molecular Devices), low-pass filtered at 10 kHz, and sampled at 20 kHz (Digidata 1440B, Molecular Devices). Pulses were delivered using a computer (Clampex 10.2 system, Molecular Devices). Patch pipettes were fabricated from borosilicate glass capillaries (Sutter Instruments, Cat. No. BF150-86-7.5) using a two-step vertical micropipette puller (PC-10; Narishige), resulting in tip resistances of 4 to 25 MΩ when filled with the intracellular solution. Patch-clamp experiments were performed with 25 biological replicates, defined as independent experimental dates. Each biological replicate included 1 to 11 technical replicates, representing individual cells patched on the same coverslip. The resting membrane potential was recorded immediately after obtaining the whole-cell configuration, without liquid junction potential

correction. To determine cell capacitance, the capacitive transient response to a –10 mV pulse was fitted with a monoexponential function. Pipette capacitance (5–7 pF) was initially compensated for, and the bridge balance was continuously checked and corrected as necessary. Series resistance was compensated for 70% or monitored throughout the experiment. Whole-cell Ca^{2+} currents were evoked using a pulse protocol consisting of a 50 to 1000-ms prepulse to –120 mV, followed by a 200-ms test pulse to –40 mV from a holding potential of –90 mV. Voltage protocols were applied every 5 to 10 s. For activation, pulses ranging from –80 mV to –20 mV were preceded by 50 ms pre-pulses to –120 mV. Steady-state inactivation was measured using a 1-s prepulse of increasing potential (from –100 to –40 mV with 10 mV increments), and the remaining channel availability after the prepulse was evaluated by a test pulse to –40 mV. Capacitive and leakage currents were subtracted online using a "P over – 4" correction procedure.

Drugs and solutions

Intracellular recordings were performed in Ames' medium (Sigma-Aldrich, Cat. No. A1420) buffered with 23 mM sodium bicarbonate (Sigma-Aldrich, Cat. No. S5761). The intracellular solution contained (in mM): 130 K-gluconate, 2 KCl, 10 Hepes, 0.2 EGTA, 2 Na$_2$ATP, and 0.3 Na$_2$GTP (∼300 mOsm), adjusted to pH 7.2 with KOH. For cesium-based intracellular solution, the composition was (in mM): 115 Cs-gluconate, 20 CsCl, 10 TEACl, 10 Hepes, 0.2 EGTA, 2 Na$_2$ATP, and 0.3 Na$_2$GTP (290–300 mOsm), adjusted to pH 7.2 with CsOH. ML218 (Sigma-Aldrich, Cat. No. SML0385) was used to block T-type Ca^{2+} channels. Additionally, TAT-C3P, a peptide specifically designed to inhibit Ca$_V$3.3 T-type Ca^{2+} channels, was synthesized and purchased from GenScript (GenScript). Peptides were dissolved in sterile water and applied to cells at a final concentration of 10 to 20 μg/ml in the culture medium for 48 h. For patch-clamp experiments, the peptide was prepared in the pipette solution at the same concentration range. All drugs and peptides were prepared from frozen stocks and dissolved in Ames' medium or the appropriate intracellular solution just before use.

RNA isolation and real-time RT-PCR

Total RNA was isolated using TRIzol reagent (Invitrogen), and 1 to 2 μg was used for complementary DNA synthesis with a high-capacity complementary DNA kit (Thermo Fisher Scientific). RT-qPCR was performed using the TaqMan Universal PCR Master Mix and TaqMan probe (Thermo Fisher Scientific). GAPDH was used as an internal control for normalization. Primer and probe sets were CACNA1G (assay ID, Hs00367969_m1), CACNA1H (Hs01103527_m1), CACNA1I (Hs01096207_m1), and GAPDH (Hs0275899_g1). PCR thermocycling conditions were 40 cycles of 20 s at 95 °C for polymerase activation, denaturation for 1 s at 95 °C, and 20 s at 60 °C for annealing/extension. Fluorescence signals were collected at the end of the elongation step of each PCR cycle (72 °C for 10 s) to monitor the quantity of amplified DNA. The

CT values were normalized to the housekeeping gene GAPDH. ΔΔCT was calculated by subtracting the ΔCT of parental cells from the ΔCT of resistant cells and calibrated using the 2-ΔΔCT method. All reactions were performed in triplicate and repeated at least three times.

Statistical analysis

Sample sizes for each experiment were determined based on previous studies (4, 9). For patch-clamp recordings, n = 25 to 68 cells were used for each condition, with cells obtained from at least three independent cultures. For qRT-PCR analyses, n = 9 to 12 independent samples were used per group. The normality of histogram parameters was evaluated using the Kolmogorov–Smirnov test. For comparisons between unpaired groups, the Mann–Whitney U test was used as data were predominantly non-parametric. For paired data, such as before and after ML218 treatment, the Wilcoxon signed-rank test was used. All statistical tests were two-sided, with significance set at $p < 0.05$. Data are presented as mean ± SD. Exact p values are reported in figures and text, along with the specific statistical test used for each analysis.

For unsupervised classification of Y79CR cells, we employed a k-means clustering algorithm. The optimal number of clusters was determined using the elbow method and silhouette analysis (Fig. S1; (25)). Statistical analyses were performed using GraphPad Prism 10 (GraphPad Software, https://www.graphpad.com) and custom routines in Igor Pro 6.3 (Wavemetrics).

Data availability

All data are located within the article. Additional data are available upon request from the corresponding author.

References

1. Abramson, D. H., Shields, C. L., Munier, F. L., and Chantada, G. L. (2015) Treatment of retinoblastoma in 2015: agreement and disagreement. *JAMA Ophthalmol.* **133**, 1341–1347
2. Dimaras, H., Corson, T. W., Cobrinik, D., White, A., Zhao, J., Munier, F. L., *et al.* (2015) Retinoblastoma. *Nat. Rev. Dis. Primers* **1**, 15021
3. Stenfelt, S., Blixt, M. K. E., All-Ericsson, C., Hallböök, F., and Boije, H. (2017) Heterogeneity in retinoblastoma: a tale of molecules and models. *Clin. Transl Med.* **6**, 42
4. Cho, C. S., Jo, D. H., Kim, J. H., and Kim, J. H. (2022) Establishment and characterization of carboplatin-resistant retinoblastoma cell lines. *Mol. Cells* **45**, 729–737
5. Liu, J., Erenpreisa, J., and Sikora, E. (2022) Polyploid giant cancer cells: an emerging new field of cancer biology. *Semin. Cancer Biol.* **81**, 1–4
6. Zhang, X., Yao, J., Li, X., Niu, N., Liu, Y., Hajek, R. A., *et al.* (2023) Targeting polyploid giant cancer cells potentiates a therapeutic response and overcomes resistance to PARP inhibitors in ovarian cancer. *Sci. Adv.* **9**, eadf7195
7. del Cerro, M., Seigel, G. M., Lazar, E., Grover, D., del Cerro, C., Brooks, D. H., *et al.* (1993) Transplantation of Y79 cells into rat eyes: an in vivo model of human retinoblastomas. *Invest. Ophthalmol. Vis. Sci.* **34**, 3336–3346
8. Howard, M. A., Dryja, T. P., Walton, D. S., and Albert, D. M. (1989) Identification and significance of multinucleate tumor cells in retinoblastoma. *Arch. Ophthalmol.* **107**, 1025–1030
9. Kim, S., Guzman, S. J., Jo, D. H., Cho, C. S., and Kim, J. H. (2021) Giant Y79 retinoblastoma cells contain functionally active T-type calcium channels. *Pflugers Arch.* **473**, 1631–1639
10. Antal, L., and Martin-Caraballo, M. (2019) T-type calcium channels in cancer. *Cancers (Basel)* **11**, 134
11. Dziegielewska, B., Casarez, E. V., Yang, W. Z., Gray, L. S., Dziegielewski, J., and Slack-Davis, J. K. (2016) T-Type Ca^{2+} channel inhibition sensitizes ovarian cancer to carboplatin. *Mol. Cancer Ther.* **15**, 460–470
12. Monteith, G. R., McAndrew, D., Faddy, H. M., and Roberts-Thomson, S. J. (2007) Calcium and cancer: targeting Ca^{2+} transport. *Nat. Rev. Cancer* **7**, 519–530
13. Phan, N. N., Wang, C. Y., Chen, C. F., Sun, Z., Lai, M. D., and Lin, Y. C. (2017) Voltage-gated calcium channels: novel targets for cancer therapy. *Oncol. Lett.* **14**, 2059–2074
14. Cui, C., Merritt, R., Fu, L., and Pan, Z. (2017) Targeting calcium signaling in cancer therapy. *Acta Pharm. Sin B* **7**, 3–17
15. Zhang, Y., Wang, H., Qian, Z., Feng, B., Zhao, X., Jiang, X., *et al.* (2014) Low-voltage-activated T-type Ca^{2+} channel inhibitors as new tools in the treatment of glioblastoma: the role of endostatin. *Pflugers Arch.* **466**, 811–818
16. Lam, R. S., Topfer, F. M., Wood, P. G., Busskamp, V., and Bamberg, E. (2017) Functional maturation of human stem cell-derived neurons in long-term cultures. *PLoS One* **12**, e0169506
17. Mongiat, L. A., Espósito, M. S., Lombardi, G., and Schinder, A. F. (2009) Reliable activation of immature neurons in the adult hippocampus. *PLoS One* **4**, e5320
18. Hirooka, K., Bertolesi, G. E., Kelly, M. E., Denovan-Wright, E. M., Sun, X., Hamid, J., *et al.* (2002) T-Type calcium channel alpha1G and alpha1H subunits in human retinoblastoma cells and their loss after differentiation. *J. Neurophysiol.* **88**, 196–205
19. McRory, J. E., Santi, C. M., Hamming, K. S., Mezeyova, J., Sutton, K. G., Baillie, D. L., *et al.* (2001) Molecular and functional characterization of a family of rat brain T-type calcium channels. *J. Biol. Chem.* **276**, 3999–4011
20. Kim, J. W., Oh, H. A., Lee, S. H., Kim, K. C., Eun, P. H., Ko, M. J., *et al.* (2018) T-type calcium channels are required to maintain viability of neural progenitor cells. *Biomol. Ther. (Seoul)* **26**, 439–445
21. Xiang, Z., Thompson, A. D., Brogan, J. T., Schulte, M. L., Melancon, B. J., Mi, D., *et al.* (2011) The discovery and characterization of ML218: a novel, centrally active T-type calcium channel inhibitor with robust effects in STN neurons and in a rodent model of Parkinson's disease. *ACS Chem. Neurosci.* **2**, 730–742
22. Cmarko, L., and Weiss, N. (2020) Selective inhibition of neuronal Ca$_V$3.3 T-type calcium channels by TAT-based channel peptide. *Mol. Brain* **13**, 95
23. Dziegielewska, B., Gray, L. S., and Dziegielewski, J. (2014) T-type calcium channels blockers as new tools in cancer therapies. *Pflugers Arch.* **466**, 801–810
24. Zhu, X., Xue, L., Yao, Y., Wang, K., Tan, C., Zhuang, M., *et al.* (2018) The FoxM1-ABCC4 axis mediates carboplatin resistance in human retinoblastoma Y-79 cells. *Acta Biochim. Biophys. Sin (Shanghai)* **50**, 914–920
25. Rousseeuw, P. J. (1987) Silhouettes: a graphical aid to the interpretation and validation of cluster analysis. *Comput. Appl. Math.* **20**, 53–65